ARTICLE

Rational design of covalent organic frameworks for efficient photocatalytic hydrogen peroxide production

Shuming Chai,[a] Xiaowen Chen,[a] Xirui Zhang,[a] Yuanxing Fang,[a]* Reiner Sebastian Sprick,[b] Xiong Chen[a]*

Hydrogen peroxide is an important chemical for environmental applications and it is also used in large-scale industrial processes. Recent studies have demonstrated photocatalytic production of H_2O_2, but the observed production rates are low making the materials not practical for application at scale. Herein, covalent organic frameworks (COFs) were studied as photocatalysts for H_2O_2 production. Two related COFs show markedly different performances, which can be explained by the presence of donor-acceptor configurations in the backbone. N_0-COF has increased charge-separation efficiencies and a better band alignment compared to its nitrogen containing analogue N_3-COF. The result is that N_0-COF has a H_2O_2 production rate of 15.7 μmol h^{-1} for 10 mg, which is ten times higher compared to N_3-COF. In this study, both experimental and theoretical studies were used to understand the improved performance. This study reveals the importance of the backbone design of metal-free materials for advanced photocatalytic applications.

Introduction

Hydrogen peroxide is an important chemical for environmental applications as it is a strong oxidant[1-3]. In addition, it is also widely used in large-scale processes in the chemical industry[4,5]. Currently, H_2O_2 is produced using the Riedl–Pfleiderer anthraquinone process which requires a catalytic hydrogenation step to form anthrahydroquinone. The process is energy intensive as uses hydrogen gas at high temperature and pressure, requires purification steps, and consumption of anthraquinone in the process makes the process environmentally problematic[6-9]. Recently, photocatalysis has been developed as a green alternative for the synthesis of H_2O_2 as it only uses water and oxygen gas as reactants, and light as energy source under mild conditions[10-12]. The reaction occurs in two sequential steps as presented in Eq (1) and (2)[13]. Oxygen gas is activated by a reduction reaction (ORR) and subsequently, the active species reacts with a photoexcited electron to form H_2O_2[14-16]. This approach avoids the use of sacrificial reagents and has therefore huge potential for scale up production[17].

$$O_2 + e^- \rightarrow \cdot O_2^- \text{ (-0.74 V vs RHE (pH=7))} \quad (1)$$
$$\cdot O_2^- + 2H^+ + e^- \rightarrow H_2O_2 \text{ (0.28 V vs RHE (pH=7))} \quad (2)$$
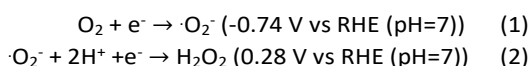
In order to produce H_2O_2 on scale, new photocatalysts have to be developed that fulfil a range of requirements: namely, light absorption profiles that match the solar spectrum[18], efficient separation of the photogenerated charge carriers[19], excellent charge transport to the surface and active sites, and high selectivity for surface reactions are required[20].

Recent studies have shown that metal-free photocatalysts can be superior to the traditional inorganic materials for this aspect, and typical examples include polymeric carbon nitride [21-24], covalent heptazine frameworks[25], covalent organic frameworks (COFs)[26,27], and others[28-30]. With respect to inorganic materials, light absorption of meta-free photocatalyst can be readily optimized by rational design of the molecular structure[31-33]. In addition, metal-free photocatalysts are favoured to proceed one-electron process, while two-electron process is avoided for hydrogen evolution reaction as shown in Eq (3)[34].

$$2H^+ + 2e^- \rightarrow H_2 \text{ (-0.41 V vs RHE (pH=7))} \quad (3)$$
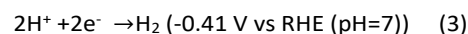
Photoexcitons in metal-free photocatalysts normally have large attractive Coulomb forces that need to be overcome limiting their charge separation efficiency. Organic materials are usually also less crystalline which limits their ability to transport charges efficiently. COF can overcome these limitations as they formed through reversible reactions yielding materials with a high degree of crystallinity[35-37]. Additionally, donor-acceptor (D-A) configurations can be induced into the molecular structure to promote charge separation[38-40]. Nevertheless, only few COFs have been reported to act as photocatalysts for H_2O_2 production.

In this study, two-dimensional COFs were designed for photocatalytic H_2O_2 production, namely N_0-COF and N_3-COF (Fig.

[a.] State Key Laboratory of Photocatalysis on Energy and Environment,College of Chemistry, Fuzhou University, Fuzhou 350116, China. E-mail: chenxiong987@fzu.edu.cn; yxfang@fzu.edu.cn

[b.] Department of Pure and Applied Chemistry, University of Strathclyde, Thomas Graham Building, 295 Cathedral Street, Glasgow G1 1XL, UK.

† Footnotes relating to the title and/or authors should appear here.

Electronic Supplementary Information (ESI) available: [details of any supplementary information available should be included here]. See DOI: 10.1039/x0xx00000x

1†). Both COFs are active for H_2O_2 production under visible light irradiation and without any sacrificial agent. In comparison, the performance of N_0-COF for H_2O_2 production is ten times higher compared to N_3-COF with a rate of ca. 15.7 μmol h^{-1} for 10 mg of the material. The improved performance can be mainly accounted to the rational design of the COF structure with the formation of a D-A configuration. This D-A structure not only promotes the separation of the photoexciton, but also affects the active sites on COF to compensate the energy barrier for H_2O_2 production. This study reveals the importance of the design of organic materials for advanced photocatalytic applications.

Results & discussion

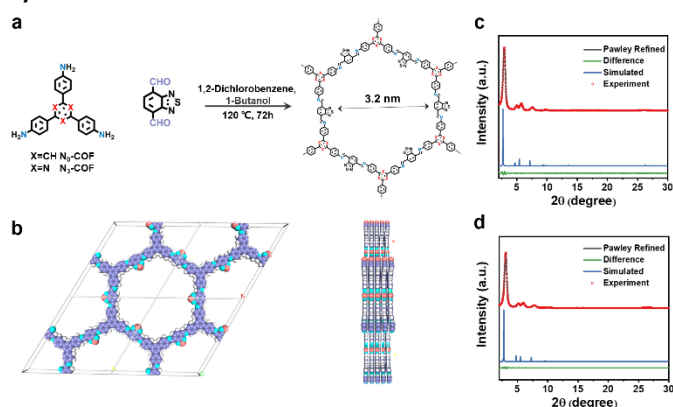### Synthesis and structural characterizations

Fig. 1 (a) Synthetic routes for N_x-COFs. (b) Top view (left) and side view (right) of the A-A packing mode of N_0-COF. (c), (d) PXRD profiles of N_0-COF (c) and N_3-COF (d).

N_0-COF and N_3-COF were synthesized by condensation of benzo[c][1,2,5]thiadiazole-4,7-dicarbaldehyde (BT-CHO) with tris(4-aminophenyl)benzene (TAPB) and tris-(4-aminophenyl)triazine (TAPTA) under solvothermal conditions (Fig. 1a, details see ESI†)[41]. Both the Fourier transform infrared (FTIR, Fig. S1-2†) and solid-state ^{13}C cross polarization-magic angle spinning nuclear magnetic resonance (^{13}C CP/MAS ssNMR, Fig. S3-4†) spectra have shown characteristic imine bond (CH=N) for these two as-prepared COFs, indicating the formation of the COFs. N 1s X-ray photoelectron spectroscopy (XPS, Fig. S5†) was further performed to distinguish the different properties of N species in the COF skeletons. The N 1s XPS profile of N_3-COF can be resolved into three major peaks centering at 398.3, 399.2, and 400.8 eV, which originates from the N species that existed in the fragments of 1,3,5-triazine rings, BT moieties, and imine bonds, respectively[42]. By contrast, the two N 1s subpeaks of N_0-COF with the binding energies of 399.3 and 401.7 eV can be assigned to the N species presented in BT units and imine linkages, respectively. These results are consistent with their FTIR and ^{13}C CP/MAS ssNMR analysis results, revealing the formation of the COF skeletons. Field-emission scanning electron microscopy (FE-SEM) images have presented the morphology of the COFs. Both of them presented rod-like structure (Fig. S6†). Thermal gravimetric analysis (TGA, Fig. S7†) shows that the COFs are stable up to 500 °C under N_2

atmosphere, indicating its high thermal-stability. Furthermore, elemental analysis results agreed well with the theoretically expected values for an infinite 2D sheet (Table S1†).

Crystallinity and porosity

Both COFs exhibited high crystallinity as evidenced by their prominent powder X-ray diffraction (PXRD) studies (Fig. 1c†). The N_0-COF material has main diffraction peaks at 2.87°, 4.87°, 5.59°, 7.37°, 9.59°, and 25.47°, corresponding to the (100), (110), (200), (210), (220), and (001) facets, respectively. Likewise, the N_3-COF material has main diffraction peaks at 2.89°, 4.91°, 5.64°, 7.42°, 9.67°, and 25.03°, which can be assigned to the (100), (110), (200), (210), (220) and (001) facets, respectively (Fig. 1d†). Structural simulation by employing eclipsed AA-stacking mode well reproduced the experimental PXRD profiles (Fig. 1c-d†), indicating both COFs adopt AA-stacking mode (Fig. 1b†). Pawley refinement (dotted black curves, Fig. 1c-d†) shows excellent agreement with the peak assignment as evident from their negligible difference (green curves, Fig. 1c-d†). In high-resolution transmission electron microscopy (HR-TEM) images (Fig. S8†), the (100) lattice plane can be observed with an interplanar spacing of 3.0 nm and 2.9 nm for N_0-COF and N_3-COF, respectively.

The porosity of the COFs was assessed by nitrogen sorption isotherm measurements performed at 77 K. Both COFs featured reversible type IV curves (Fig. S9†), signifying the presence of mesopores among the COFs. The specific Brunauer-Emmett-Teller (BET) surface areas were determined to be 1356 m^2 g^{-1} for N_0-COF and 1062 m^2 g^{-1} for N_3-COF, respectively. The surface area is much larger than other traditional photocatalysts. Furthermore, the pore size distributions of both COFs were evaluated by using the nonlocal density functional theory method, yielding the dominant peak centered at 3.38 nm and 3.36 nm for N_0-COF and N_3-COF, respectively (Fig. S10†).

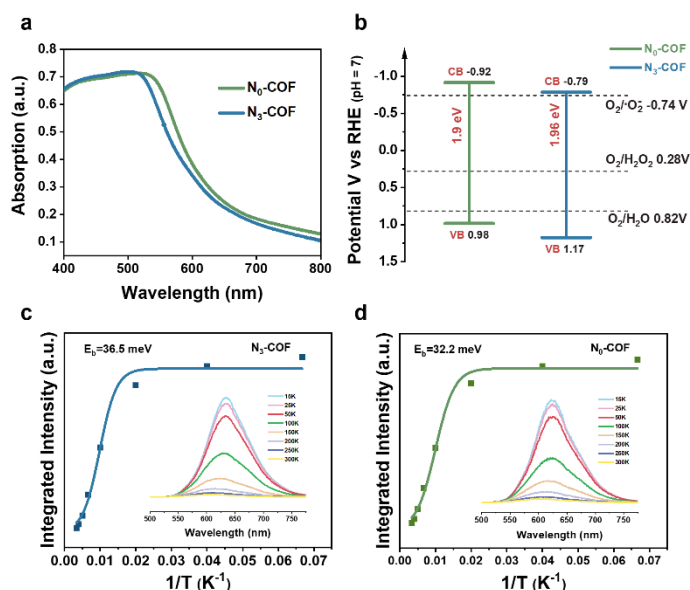### Optical and photophysical properties

Fig. 2 (a) UV-vis DRS of COFs in the solid state. (b) Band structures of COFs. (c), (d) Integrated photoluminescence emission intensity as a function of temperature-dependent photoluminescence spectra of N_0-COF (c), and N_3-COF (d), λ_{ex}=450 nm.

The optical properties of the COFs were studied by ultraviolet-visible diffuse reflectance spectra (UV-vis DRS) as shown in Fig. 2a. The absorption edges of both COFs are similar, closing to 550 nm. On basis of these results, the optical bandgaps (E_g) of these two COFs are calculated to be 1.9 eV and 1.96 eV for N_0-COF and N_3-COF, respectively (Fig. S11†). N_0-COF was observed with a slightly bathochromic shift owing to the formation of D-A architecture, and thus, light absorption and energy utilization can be promoted. DFT calculations were further carried out to investigate the optical characteristic of the catalysts (Fig. S12†). The highest occupied molecular orbital (HOMO) of N_3-COF is the $n \rightarrow \pi^*$ transition, which preferably leads to transition prohibition, resulting in a lower light-harvesting ability than N_0-COF with $\pi \rightarrow \pi^*$ transition[43]. In contrast, the lowest unoccupied molecular orbitals (LUMOs) of both COFs are mainly delocalized on the BT fragments. Accordingly, the HOMO-LUMO gaps by the DFT calculation are 2.14 eV and 2.25 eV for N_0-COF and N_3-COF, respectively. These results are consistent with the experiment that N_0-COF possesses broader light absorption than N_3-COF. Besides, derived from the Mott-Schottky profiles (Fig. S13†), the flat-band potentials of N_0-COF and N_3-COF are estimated to be -0.7 and -0.57 V, respectively. Combining E_g with Mott-Schottky plots, the band structures of both COFs are portrayed (Fig. 2b†). As such, both COFs are capable of driving ORR and subsequently to synthesize H_2O_2. Meanwhile, the photoexcitation hole is capable of driving water oxidation reaction. Noted that with respect to the N_3-COF, the CB of N_0-COF is supposed to present an improved performance for H_2O_2 production.

Temperature-dependent photoluminescence (PL) spectra of both COFs were recorded to study exciton dissociation efficiencies. As shown in Fig. 2c-d, both COFs demonstrated thermal quenching of their PL emission in the temperature range from 15 to 300 K. Accordingly, by fitting the data of relevant PL peak intensity in different temperatures, the corresponding E_b can be estimated by using the Arrhenius equation, $I(T)=I_0/(1+A \exp(-E_b/k_bT))$. The E_b of N_0-COF (32.2 meV) is lower than that of N_3-COF (36.5 meV), which can be ascribed to the extended conjugation in the scaffold for N_0-COF resulting from a D-A configuration[38, 44]. The push-pull effect between the donor (TAPB) and acceptor (BT) unit is likely lowering the electrostatic Coulomb attraction of charge carriers, enabling enhanced exciton separation, which increases photocatalytic activity of N_0-COF[45].

It is noteworthy to mention that the ambipolar segregated D and A channels in the 2D D-A COF enable the interlayer transport of holes and electrons through the aligned D-on-D and A-on-A periodical columns via π-π interactions. In combining with the intralayer directional charge transfer from D to A motif, a D-A type COF (N_0-COF here) is believed to present boosted charge carrier transport rates and photoelectric responsiveness due to the combination of holes and electrons migration compared to a common COF material (N_3-COF here)[46], which is beneficial to the improvement of photocatalytic

efficiency. Room temperature electron paramagnetic resonance (EPR) spectroscopy was used to probe unpaired electrons in both COFs[47]. As displayed in Fig. S14†, it was evident that N_0-COF represented a stronger EPR signal than N_3-COF, on account of N_0-COF equipped with sufficient free charge carriers, which can markedly stimulate ORR[48]. Moreover, time-resolved photoluminescence (PL) decay spectra and transient photocurrent response were evaluated to explore the charge migration ability. The exciton lifetime and the charge separation behaviors of the N_0-COF and N_3-COF were first clarified by time-resolved PL decay measurements. By comparison, the decay kinetics for N_3-COF was much faster than those of N_0-COF, with average emission lifetimes estimated to be 1.98 and 0.51 ns for N_0-COF and N_3-COF, respectively (Fig. S15†). The longer PL lifetime for N_0-COF increases the possibility of electrons to be involved in the proton reduction reaction. In addition, the transient photocurrent responses were measured by the on-off cycles under visible light irradiation. As shown in Fig. S16†, the value of photocurrent response is about three times higher for N_0-COF than N_3-COF, indicating greater reaction activities took place in N_0-COF, which agrees with our assumption[49]. The linear sweep voltammetry (LSV) curves of the COF-based photoelectrodes are presented in Fig. S17†. It is obvious that when the light is on, both COF photoelectrodes have presented photocurrent density, and the performance of N_0-COF is better than N_3-COF, agreeing with the performance of H_2O_2 production by powder COF materials. All taken together, we therefore expected that N_0-COF exhibits higher activity than N_3-COF for photocatalytic production of H_2O_2.

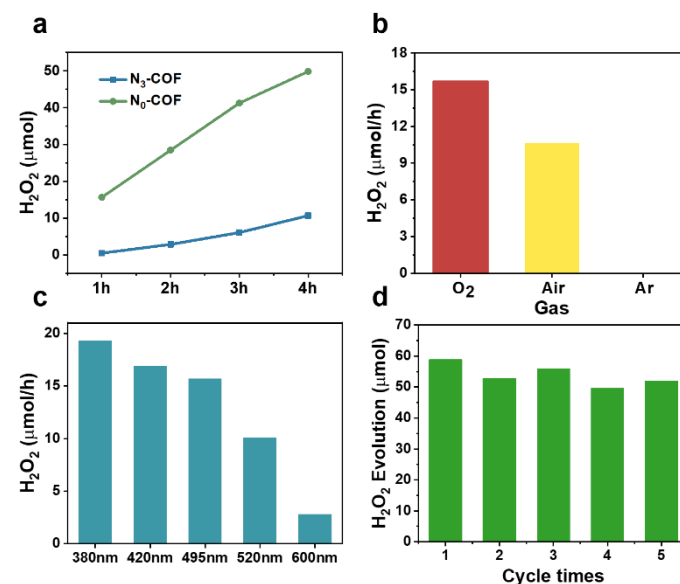## Photocatalytic H_2O_2 production

Fig. 3 (a) The reaction photocatalytic activities of N_0-COF and N_3-COF within over a 4 hours period. (b), (c) The reaction activities of N_0-COF under different atmospheres (b) and different wavelengths (c). (d) The reaction activity of N_0-COF for 5 four-hour cycles times (total 20 h).

Photocatalytic H_2O_2 evolution was performed in sealed Schlenk tubes with 10 mg COF photocatalyst in pure H_2O under monochromatic light (495 nm LED) irradiation (details see ESI†).

As shown in Fig. 3a, both COFs showed photoactivity for H_2O_2 production, and the amount increased steadily with prolonged irradiation time. Notably, N_0-COF achieves an average photocatalytic H_2O_2 production rate (HPPR) of 15 µmol h^{-1}, which is appropriately 10 times to N_3-COF. It is important to note that photocatalytic H_2O_2 production coupled to ORR by COFs has rarely been explored so far and the performance here surpasses most of the reported COFs (e.g., TAPD-(Me)$_2$ COF has presented H_2O_2 production rate ca. 4.6 µmol h^{-1})[26] (Table S2†)[27]. The high photocatalytic activity of N_0-COF mainly arises from the promoted light-harvesting ability, increased charge carrier dissociation efficiency, and faster charge transfer, closely related to the D-A structure. To unravel the H_2O_2 production pathway during photocatalysis, we further conducted the reaction in different atmospheres. As illustrated in Fig. 3b, the HPPR for N_0-COF was highest under pure O_2 atmosphere, significantly lowered under air, and completely inhibited under Ar. This strongly suggests that H_2O_2 was produced via the pathway from Eq 1 and 2.

Besides, the effect of different irradiation wavelengths on the photocatalytic HPPR for N_0-COF was studied (Fig. 3c†). Interestingly, N_0-COF shows high photoactivity over a wide range and even remained active at 600 nm, which is a result of its broad optical absorption. Moreover, the stability of N_0-COF was evaluated through repeated cycling experiments. As shown in Fig. 3d, no significant decrease of H_2O_2 production rate was observed over 5 cycles. In addition, no apparent difference of the COF either from the FE-SEM images or the FT-IR spectra after repeated cycling experiments was observed (Fig. S17-18†), suggesting good photocatalytic stability of N_0-COF.
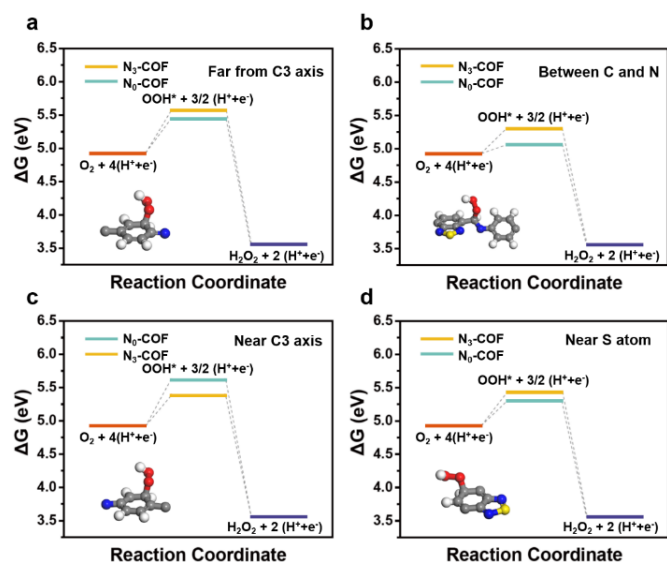
Reaction mechanism exploration

Fig. 4 DFT calculated free energy diagrams of oxygen reduction pathways toward H_2O_2 generation on different active sites in N_0-COF and N_3-COF: far from C3 axis (a); between C and N (b); near C3 axis (c); near S atom (d).

Further control experiments were performed to study the reaction mechanism. No H_2O_2 generation was detected when the reaction was conducted without the COF photocatalyst. Furthermore, no H_2O_2 was produced in the dark or under Ar atmosphere. This emphasizes the essential roles of the COF as the photocatalyst, requiring light and oxygen gas for the photocatalytic production of H_2O_2. When benzoquinone was used as a radical scavenger in the reaction system, no formation of H_2O_2 was observed (Table S3†). This shows that radicals for H_2O_2 play a role in the mechanism, as expected in the sequential two-step single-electron indirect reduction and OO* radical formation as reaction intermediates in the ORR. The presence of OO* radicals were further confirmed by trapping experiments. A distinct characteristic EPR signal for OO* centered at around 3510 G was observed when exposed to visible light after the introduction of 5,5-dimethyl-1-pyrroline N-oxide (DMPO) adduct (Fig. S19†).
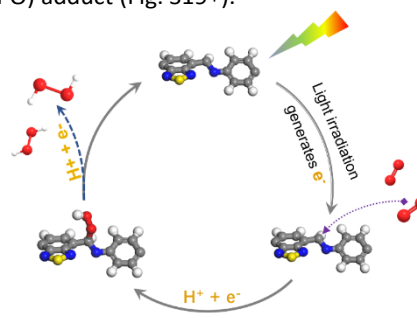

Fig. 5 A proposed plausible mechanism for photocatalytic H_2O_2 production via ORR.

Further, the possible reactive sites for ORR were predicted by DFT calculations. In a typical sequential two-step single-electron indirect reduction process, O_2 first accepts one electron to generate the OO* intermediates, which are the critical step to produce H_2O_2. As shown in Fig. 4 and Table S4-5, the OO* in the connection between two moieties (*i.e.* imine bond) for both COFs features favorable Gibbs free energy change (ΔG) compared to other sites. Thus, this seat is likely to serve as an active site for photocatalytic ORR. Meanwhile, in the case of N_0-COF, there is a lower energy barrier to form the OO* radicals. Though in both COFs, the activity site is supposed to be same position, the formation of D-A configurate in N_0-COF affects the atomic orbital and compensates the energy barrier for H_2O_2 production. This illustration is an important hint for its high reaction activity. Meanwhile, the valence band potential of the COF cannot drive H_2O_2 production since the valence band are 1.26 V for N_0-COF and 1.42 V for N_3-COF, which are lower than 1.76 V vs RHE. Therefore, O_2 is the only possible product to be achieved. To clarify this understanding, we have performed a half oxidation reaction using this photocatalyst and electrode sacrifice agent Ag^+. O_2 gas can be readily collected and the yield of O_2 was 7.8 µmol h^{-1}, but not any H_2O_2. In addition, without any O_2 gas input, we cannot detect any H_2O_2 as shown in Fig. S20†. This observation also confirms that the H_2O_2 production reaction is performed by reductive reaction using photoexcitation electron, and O_2 evolution is conducted on the oxidation side. Based on these results, a plausible mechanism for H_2O_2 production via ORR is proposed (Fig. 5†).

Journal Name

ARTICLE

Conclusions

In summary, 2D COF with different configurations were studied for photocatalytic H_2O_2 production in pure water. Through rational design of the COF structure, the production of H_2O_2 can be significantly increased by 10-fold. The relationship between the performance and structure was investigated through both experimental and computational approaches. The improved performance can be mainly ascribed to the formation of D-A structure, since it not only promotes the separation of the photoexcitation charges, but also affect the active site to compensate for the energy barrier. This study shows a new approach in the rational design of metal-free materials for advanced photocatalytic applications.

Conflicts of interest

There are no conflicts to declare.

Acknowledgements

References

1. K. Oka, H. Nishide and B. Winther-Jensen, *Adv. Sci.*, 2021, **8**, 2003077.
2. M. Miwako Teranishi, S.-i. Naya and H. Tada, *J. Am. Chem. Soc.*, 2010, **132**, 7850–7851.
3. Z. Teng, W. Cai, W. Sim, Q. Zhang, C. Wang, C. Su and T. Ohno, *Appl. Catal. B: Environ.*, 2021, **282(2021)**, 119589.
4. S. A. Mousavi Shaegh, N.-T. Nguyen, S. M. Mousavi Ehteshami and S. H. Chan, *Energy Environ. Sci.*, 2012, **5**, 8225.
5. L. Wang, J. Zhang, Y. Zhang, H. Yu, Y. Qu and J. Yu, *Small*, 2021, **2104561**.
6. Y. Gao, W. Zhu, Y. Li, Q. Zhang, H. Chen, J. Zhang and T. Huang, *J. Environ. Manage*, **304 (2022)** 114315.
7. T. Liu, X. Meng, Y. Wang, X. Liang, Z. Mi, X. Qi, S. Li, W. Wu, E. Min and S. Fu, *Ind. Eng. Chem. Res.*, 2004, **43**, 166-172.
8. E. S. Shanley, *J. Chem. Educ.*, 1948, **25**, 180.
9. J. M. Campos-Martin, G. Blanco-Brieva and J. L. G. Fierro, *Angew. Chem. Int. Ed.*, 2006, **45**, 6962 – 6984.
10. Y. Fang, Y. Hou, X. Fu and X. Wang, *Chem. Rev.*, 2022, DOI: 10.1021/acs.chemrev.1c00686.
11. G. Zhang, Z.-A. Lan, L. Lin, S. Lin and X. Wang, *Chem. Sci.*, 2016, **7**, 3062-3066.
12. J. Shi, T. Yuan, R. Wang, M. Zheng and X. Wang, *Green. Chem.*, 2021, **23**, 3945.
13. W. Zhang, X. Chenb, X. Zhaoa, M. Yina, L. Fengb and H. Wang, *Appl. Surf. Sci.*, 2020, **527 (2020)**, 146908.
14. L. Xu, Y. Liu, L. Li, Z. Hu and J. C. Yu, *ACS Catal.*, 2021, **11**, 14480–14488.
15. Y. Xue, Y. Wang, Z. Pan and K. Sayama, *Angew. Chem. Int. Ed.*, 2021, **60**, 10469 –10480.
16. Z. Teng, Q. Zhang, H. Yang, K. Kato, W. Yang, Y.-R. Lu, S. Liu, C. Wang, A. Yamakata, C. Su, B. Liu and T. Ohno, *Nat. Catal.*, 2021, **4**, 374-384.
17. L. Yang, H. Chen, Y. Xu, R. Qian, Q. Chen and Y. Fang, *Chem. Eng. Sci.*, 2022, **251**, 117435.
18. X. Li, J. Wang, Y. Fang, H. Zhang, X. Fu and X. Wang, *Acc. Mater. Res.*, 2021, **2, 10**, 933–943.
19. Y. Fang, Y. Xu, X. Li, Y. Ma and X. Wang, *Angew.Chem. Int.Ed.*, 2018, **58**, 9749 –9753.
20. L. Wang, P. Cai, Z. Liu, Z. Xie and Y. Fang, *J. Colloid Interface Sci.*, **607 (2022)**, 203–209.
21. Y. Kofuji, Y. Isobe, Y. Shiraishi, H. Sakamoto, S. Tanaka, S. Ichikawa and T. Hirai, *J. Am. Chem. Soc.*, 2016, **138**, 10019-10025.
22. X. Zeng, Y. Liu, Y. Kang, Q. Li, Y. Xia, Y. Zhu, H. Hou, M. H. Uddin, T. R. Gengenbach, D. Xia, C. Sun, D. T. Mccarthy, A. Deletic, J. Yu and X. Zhang, *ACS Catal.*, 2020, **10**, 3697–3706.
23. C. Chu, Q. Zhu, Z. Pan, S. Gupta, D. Huang, Y. Du, S. Weon, Y. Wu, C. Muhich, E. Stavitski, K. Domen and J. H. Kim, *Proc. Natl. Acad. Sci. U.S.A.*, 2020, **117**, 6376-6382.
24. H. Ou, C. Tang, X. Chen, M. Zhou and X. Wang, *ACS Catal.*, 2019, **9**, 2949-2955.
25. H. Cheng, H. Lv, J. Cheng, L. Wang, X. Wu and H. Xu, *Adv. Mater.*, 2021, **2107480**
26. C. Krishnaraj, H. Sekhar Jena, L. Bourda, A. Laemont, P. Pachfule, J. Roeser, C. V. Chandran, S. Borgmans, S. M. J. Rogge, K. Leus, C. V. Stevens, J. A. Martens, V. Van Speybroeck, E. Breynaert, A. Thomas and P. Van Der Voort, *J. Am. Chem. Soc.*, 2020, **142**, 20107-20116.
27. F. Tan, Y. Zheng, Z. Zhou, H. Wang, X. Dong, J. Yang, Z. Ou, H. Qi, W. Liu, Z. Zheng and X. Chen, *CCS Chem.*, 2022, DOI: 10.31635/ccschem.022.202101578.
28. Y. Isaka, Y. Kawase, Y. Kuwahara, K. Mori and H. Yamashita, *Angew. Chem. Int. Ed.*, 2019, **58**, 5402-5406.
29. W. Hou, Y. Li, S. Ouyang, H. Chen, J. Ye, X. Han and Y. Deng, *Chem. Commun.*, 2019, **55**, 13279-13282.
30. Y. Kawase, Y. Isaka, Y. Kuwahara, K. Mori and H. Yamashita, *Chem. Commun.*, 2019, **55**, 6743-6746.
31. M. L. Sun, Y. R. Wang, W. W. He, R. L. Zhong, Q. Z. Liu, S. Xu, J. M. Xu, X. L. Han, X. Ge, S. L. Li, Y. Q. Lan, A. M. Al-Enizi, A. Nafady and S. Ma, *Small*, 2021, DOI: 10.1002/smll.202100762, 2100762.
32. G. Ji, Z. Yang, X. Yu, Y. Zhao, F. Zhang and Z. Liu, *ACS Sustainable Chem. Eng.*, 2020, **8, 43**, 16320–16326.
33. C. Yang, W. Huang, L. C. da Silva, K. A. I. Zhang and X. Wang, *Chem. Eur. J.*, 2018, **24**, 17454-17458.
34. S. B. Yang, Y. J. Gong, J. S. Zhang, L. Zhan, L. L. Ma, Z. Y. Fang, R. Vajtai, X. C. Wang and P. M. Ajayan, *Adv. Mater.*, 2013, **25**, 2452-2456.
35. F. Wang, J. Zhang, Y. Shao, H. Jiang, Y. Liu and R. Chen, *Ind. Eng. Chem. Res.*, 2020, **59**, 18489-18499.
36. F. J. Uribe-Romo, C. J. Doonan, H. Furukawa, K. Oisaki and O. M. Yaghi, *J. Am. Chem. Soc.*, 2011, **133**, 11478-11481.
37. J. Ming, A. Liu, J. Zhao, P. Zhang, H. Huang, H. Lin, Z. Xu, X. Zhang, X. Wang, J. Hofkens, M. B. J. Roeffaers and J. Long, *Angew. Chem. Int. Ed.*, 2019, **58**, 18290-18294.
38. Z.-A. Lan, G. Zhang, X. Chen, Y. Zhang, K. A. I. Zhang and X. Wang, *Angew. Chem. Int. Ed.*, 2019, **58**, 10236 –10240.
39. F. Yang, C.-C. Li, C.-C. Xu, J.-L. Kan, B. Tian, H.-Y. Qu, Y. Guo, Y. Geng and Y.-B. Dong, *Chem. Commun.*, 2022, **58**, 1530.

40.   S. Zang, G. Zhang, P. Yang, D. Zheng and X. Wang, *Chem. Eur. J.*, 2019, **25**, 6102-6107.
41.   W. Chen, Z. Yang, Z. Xie, Y. Li, X. Yu, F. Lu and L. Chen, *J. Mater. Chem. A*, 2019, **7**, 998-1004.
42.   J. Xu, C. Yang, S. Bi, W. Wang, Y. He, D. Wu, Q. Liang, X. Wang and F. Zhang, *Angew. Chem. Int. Ed.*, 2020, **59**, 23845-23853.
43.   Y. Chen, B. Wang, S. Lin, Y. Zhang and X. Wang, *J. Phys. Chem. C*, 2014, **118**, 29981–29989.
44.   Z.-A. Lan, M. Wu, Z. Fang, X. Chi, X. Chen, Y. Zhang and X. Wang, *Angew. Chem. Int. Ed.*, 2021, **60**, 16355 –16359.
45.   Y. Yu, C. Cao, H. Liu, P. Li, F. Wei, Y. Jiang and W. Song, *J. Mater. Chem. A*, 2014, **2**, 1677–1681
46.   X. Feng, L. Chen, Y. Honsho, O. Saengsawang, L. Liu, L. Wang, A. Saeki, S. Irle, S. Shu, Y. Dong and D. Jiang, *Adv. Mater.*, 2012, **24**, 3026–3031.
47.   G. G. Zhang and X. C. Wang, *J. Catal.*, 2013, **307**, 246-253.
48.   G. Li, Z. Xie, S. Chai, X. Chen and X. Wang, *Appl. Catal. B: Environ.*, 2021, **283**, 119637.
49.   Z. Pan, G. Zhang and X. Wang, *Angew.Chem. Int. Ed.*, 2019, **58**, 7102 –7106.